

The lightcurve intrinsic variability in 47 Kepler contact binary stars

B. Debski[★]

Astronomical Observatory, Jagiellonian University, Orla 171, 30-244 Krakow, Poland

Accepted XXX. Received YYY; in original form ZZZ

ABSTRACT

This work studies the significance of the lightcurve intrinsic variability in the numerical modeling of contact binaries. Using synthetic light curves we are showing that the starspot-based intrinsic variability increases the apparent mass ratio by $\Delta q = 5\%$. For systems with orbital period $P > 0.3$ d the effect of intrinsic variability averaged over long time cancels each other out with the Kepler Mission-like phase smearing. Further, we analyse 47 totally eclipsing Kepler Mission contact binaries. We found a sharp cutoff of the intrinsic variability at $P = 0.45$ d. With the light curve numerical modeling and observational relations we derive physical parameters of the 47 systems. At least 53% of binaries have a possible third companion. 21 binaries show the O’Connell effect in the averaged phase curve. 19 of them have a primary maximum lower than the secondary, suggesting a stationary dark region on the trailing side. Using the $P = 0.45$ d cutoff we propose a new approach on the Period-Color relation. The only parameter correlating with the magnitude of the intrinsic variability is the apparent effective temperature ratio. We conclude that instead of describing the system parameters, the A/W-subtype division should be applicable only to the lightcurves, as a tentative phenomenon.

Key words: stars: activity – binaries: close – binaries: eclipsing

1 INTRODUCTION

Contact binary stars of the W UMa-type are one of the most interesting examples of close binaries. According to their canonical model (Lucy 1968a,b), they consist of two main sequence stars, which share a common convective envelope. Following the Roche geometry, the contact configuration means that both components exceed their Roche lobes and the common surface of a binary lies somewhere between the inner and outer critical Lagrangian equipotential surfaces. The Roche geometry itself is controlled via one parameter only: the mass ratio of the binary components (see Kopal 1959). With a shared surface and only one parameter driving the geometry, the process of numerical modeling of the lightcurves of contact binaries is relatively straightforward. As a direct consequence of that, there is large number of publications with contact binary models. Great many of them utilizing the Wilson-Devinney code (Wilson & Devinney 1971) or its adaptations (such as Phoebe¹). Such systems are proven to last for a very long time, reaching even a few billions of years, before final merging (Webbink 2003; Gazeas & Stępień 2008). Their slow, quasi-stable evolution is explained well by the Thermal Relaxation Oscillations theory (Flannery 1976; Lucy 1976).

Despite a long history of observations, rich bibliography and a multitude of case study lightcurve models, the interiors of contact binaries are still rather poorly understood. Even the surface itself

remains a conundrum. For example, the common convective envelope should have a, more or less, uniform effective temperature. This follows, the lightcurves of contact binaries should have primary and secondary minima of nearly equal depths. Observations show that this holds even for the most extreme mass ratios (such as $q = 0.044$, see Samec et al. 2018). While such situation is true in general, the lightcurves of contact binaries tend to exhibit significant intrinsic variations. The same intrinsic variations are causing the time dependent short-scale minima timing variations (Tran et al. 2013) and variations of the O’Connell effect (see e.g. Debski 2020). This phenomenon is being explained collectively with the presence of starspots (the ‘subluminous regions’ in Binnendijk 1965). Mullan (1975) pointed out that such phenomena can be of magnetic origin. But the problem with the starspot-based intrinsic variability is that in order to make the starspot migrate, a differential rotation should be introduced. How to merge the necessity of a differential rotation with the canonical model of contact binaries is not fully resolved yet. Nonetheless, the existence of starspots leads to some interesting scenarios, such as estimating the thickness of the convective zone, basing on the spot coverage. Starspots could be therefore used as a probing tool for introductory studies of the interiors of contact binaries.

The general issue with that approach lies within the reliability of the spot parameters. Usually, spots are introduced in the numerical modeling as a circular region on one of the stars. They are defined by their position (longitude and co-latitude), relative temperature, and radius (e.g. in the Wilson-Devinney code as of Wilson 1979). Out of those four parameters only the longitudinal position can be recovered reliably. The size of a spot and its distance from

[★] E-mail: b.debski@oa.uj.edu.pl

¹ <http://phoebe-project.org>

the stellar pole are so highly entangled, that it is practiced by many to just fix the position of the spot on the equator. Such an approach, while greatly reduces the computational time, is obviously based on no physical premises. In the end, the resulting model is not quite useful when it comes to analyze the spot itself.

With this article we begin our study of the lightcurve intrinsic variability understood as a direct consequence of the photospheric phenomena. Our general approach is to treat the intrinsic variability as a tool for testing the starspot migration models. We study the 'evolution of the lightcurve', as shown in the preliminary works in [Debski et al. \(2014, 2015\)](#) and [Debski \(2020\)](#). Such initiative was possible only with the release of a multitude of the long time-base, precise lightcurves provided by the Kepler mission ([Borucki et al. 2010](#)). Our methods and the resulting catalog of lightcurve intrinsic variability in more than 1200 objects are to be described elsewhere². This work is focused on building a primary set of contact binaries, with well established system parameters. One of the main parts of this endeavour is the analysis of how the intrinsic variability can influence the results of the numerical modeling in case of contact binaries. Hence, we begin this work with an introduction of how the averaging of the intrinsic variability affect a phase-folded lightcurve. In the next step, we analyse the intrinsic variability averaging combined with the phase smearing ([Zola et al. 2017](#)). The numerical modeling scheme and resulting models are shown in Section 5. In the final part we explore the physical parameters of the objects and discuss the results in the light of recent literature.

2 SAMPLE SELECTION

We composed the set of contact binary candidates using the Kepler Eclipsing Binary Catalogue³ (hereafter *KEBC*, [Prša et al. 2011](#)). The initial selection of objects was limited by the morphology parameter $0.6 \leq \rho \leq 1.0$ (see [Matijević et al. 2012](#)). From there, we chose objects with the difference between the minima depths smaller than $\delta_{min} = 0.1$ in the units of the normalized flux. Next, we selected the objects flagged with the flat-bottom minimum (flag *FB* in *KEBC*). This criterion is vital from the perspective of lightcurve numerical modeling. [Terrell & Wilson \(2005\)](#) showed that the presence of a total eclipse in a contact binary allows to recover its mass ratio and inclination with a very high certainty. This allowed us to study the selected objects without the necessity of having their spectroscopic mass ratios.

After downloading the lightcurves we conducted a visual inspection. For that we used the already detrended flux provided in *KEBC*. The visual inspection was possible with a prior phase-folding of each lightcurve. We adopted a bin width of approx. 12 orbital periods. The exact number of orbital periods used in this procedure varied at each object, as the lightcurves tend to experience different rates of intrinsic variability. Afterwards, because of the possible third light contamination, we gradually tightened the constraint on δ_{min} . The extend of the constraint was determined individually per object, largely depending on the width of the flat-bottom minimum. This left us with a final set of 47 objects, of which study we present here.

² A preliminary preview of the catalog is possible at <http://bade.space/lcma/>

³ <http://keplerebs.villanova.edu/>, accessed in February 2019

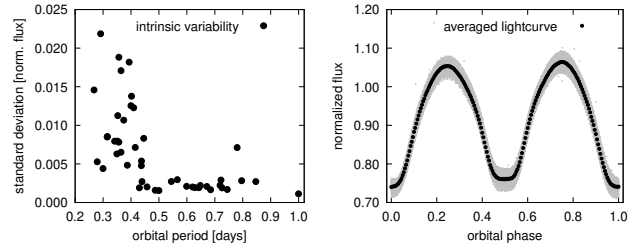


Figure 1. The intrinsic variability of lightcurves in our sample. The right panel shows an example of how the intrinsic variability produces a data scattering a phased lightcurve of KIC 2159783. The phased lightcurve (grey dots) is superimposed with its averaged counterpart (black dots). The left panel shows the distribution of the intrinsic variability along the orbital period for objects in our sample. The intrinsic variability was measured here as the standard deviation of the residuals left after subtracting the averaged lightcurve from the phased data.

Table 1. Modeling results of the light curve distorted by an averaged longitudinal spot migration (SMA). The results are grouped by column, e.g. column one contains the results for the system with an input mass ratio $q = 0.10$. The values are given in a relative form, i.e. as the ratio of the parameter value after the modeling to the input one. The apparent mass ratio and inclination are greater than their input counterparts, regardless the initial mass ratio. The apparent fill-out factor is significantly enlarged for the smallest input mass ratio only. The secondary component effective temperature is not affected by the SMA whatsoever.

q (model)	0.10	0.20	0.30
Δi	1.03	1.03	1.02
ΔT_2	1.00	1.00	1.00
$\Delta f f$	1.11	1.01	1.00
Δq	1.05	1.05	1.05

3 SOFTWARE

The numerical modeling performed in this work utilized a modified Wilson-Devinney code. In our version of the code, the differential correction mechanism was replaced with a controlled Monte Carlo method. The same code was used earlier in, e.g., [Zola et al. \(2010\)](#); [Debski et al. \(2014, 2015\)](#); [Debski \(2019, 2020\)](#). For the numerical simulations we used a lightcurve generator based on the same version of the modified Wilson-Devinney code. This code is still using monochromatic wavelengths. Each and every contact binary model in this work assumes a square root limb darkening law with the limb darkening coefficients taken from [Claret & Bloemen \(2011\)](#); [Claret et al. \(2013\)](#). The gravitational brightening coefficient was fixed to $\beta = 0.08$ ($g = 0.32$).

4 THE LIGHTCURVE INTRINSIC VARIABILITY

An average Kepler mission lightcurve consists of about 65 000 datapoints, which, for a typical contact binary system, translates into about 4 000 orbital epochs. A standard approach towards the numerical modeling of such a lightcurve require a prior phase folding and averaging. The result is a very convenient reduction of the number of datapoints. Only in such a way the numerical modeling codes (e.g. the W-D code) can work within the reasonable time limits. But phase folding over such many orbital epochs may cause the resulting phased lightcurve to be burdened with trace distortions that come

Table 2. Modeling results for the light curve distorted by the phase smearing effect (PS). The values are presented in the same relative fashion as in Table 1. Results in this table are grouped by the input mass ratio. The columns represent subsequent runs with an increasing orbital period simulated in the light curve smearing. The modeling process did not take into account the phase smearing. Interestingly, the Δq values are very similar in between the input mass ratios, unlike the Δi and $\Delta f f$, which are affected the most for the lowest input mass ratios. PS does not affect the secondary component apparent effective temperature.

	P_{orb} [d]	0.25	0.30	0.35	0.40	0.60	0.80
$q = 0.1$	Δi	0.88	0.93	0.95	0.95	0.97	0.99
	ΔT_2	1.00	1.00	1.00	1.00	1.00	1.00
	$\Delta f f$	5.48	3.17	2.43	2.43	1.80	1.21
	Δq	0.85	0.92	0.94	0.94	0.97	0.99
$q = 0.2$	Δi	0.92	0.95	0.96	0.96	0.99	0.99
	ΔT_2	1.00	1.00	1.00	1.00	1.00	1.00
	$\Delta f f$	3.23	2.26	2.16	2.16	1.29	1.07
	Δq	0.88	0.93	0.95	0.95	0.98	0.99
$q = 0.3$	Δi	0.95	0.96	0.97	0.97	0.99	1.00
	ΔT_2	1.00	1.00	1.00	1.00	1.00	1.00
	$\Delta f f$	2.63	2.07	1.76	1.76	1.28	1.05
	Δq	0.86	0.92	0.94	0.94	0.98	0.99

Table 3. Modeling results for the light curves distorted by both the phase smearing (PS) and the spot migration averaging (SMA) effects. The design of this table is exactly the same as Table 2. The modeling did not account for the PS nor the SMA effects. For binaries with $P \geq 0.3$, both PS and SMA are largely complementing each other in the mass ratio domain.

	P_{orb} [d]	0.25	0.30	0.35	0.40	0.60	0.80
$q = 0.1$	Δi	0.90	0.94	0.96	0.96	0.99	1.03
	ΔT_2	1.00	1.00	1.00	1.00	1.00	1.00
	$\Delta f f$	5.16	3.01	2.43	2.44	1.77	1.15
	Δq	0.91	0.97	1.00	1.00	1.02	1.04
$q = 0.2$	Δi	0.94	0.96	0.98	0.98	1.00	1.03
	ΔT_2	1.00	1.00	1.00	1.00	1.00	1.00
	$\Delta f f$	3.08	2.48	1.97	1.97	1.39	1.04
	Δq	0.93	0.97	1.00	1.00	1.03	1.04
$q = 0.3$	Δi	0.96	0.98	0.99	0.99	1.00	1.02
	ΔT_2	1.00	1.00	1.00	1.00	1.00	1.00
	$\Delta f f$	2.80	2.02	1.67	1.67	1.44	1.00
	Δq	0.91	0.97	1.00	1.00	1.02	1.04

from a short-time scale intrinsic variability. It is usually assumed that the process of averaging will safely remove any unwanted signal, as the intrinsic variability will cancel itself out over a long period of time. Or at least its impact will be minimized to the point of it being negligible. We decided to challenge this assumption.

To start with, we measured the magnitude of the intrinsic variability occurring over four years of Kepler mission, for the objects in our sample. In the most basic way, the intrinsic variability can be expressed as a standard deviation of residuals left after subtracting the averaged lightcurve from the phase-folded data. A discussion on this method, as well as a presentation of an alternative approach, is available in the Appendix A. We established that in our sample the intrinsic variability becomes an important factor in objects with orbital period $P < 0.45$ d. Interestingly, for objects with $P > 0.45$ d the intrinsic variability is almost negligible. As shown in the left panel of Fig. 1, the $P = 0.45$ d boundary divides the sample with

a sharp cut-off. While this boundary is interesting by itself, we decided to tackle its physical implications in an another study.

A proper analysis of the Kepler lightcurve distortions has to acknowledge the 0.5 hour integration time of the Kepler Long Cadence mode, which introduces the ‘phase smearing’ effect. Its impact on a lightcurve can partially be taken into account when using the newest versions of the original W-D code. Zola et al. (2017) showed that for contact binaries with orbital period shorter than $P = 0.4$ d it is absolutely imperative to take into account the phase smearing effect during the numerical modeling of the Kepler Mission lightcurves. We will revisit that analysis in this Section, as well as confront the lightcurve smearing with the averaging of the intrinsic variability.

To quantify the impact of the intrinsic variability averaging on the numerical modeling results, we devised a set of modeling runs based on three synthetic contact binaries. The simulated systems were differing in mass ratios: $q = 0.10, 0.20, 0.30$ and had otherwise identical system parameters: $i = 85^\circ$, $T_1 = T_2 = 6000$ K, $ff = 0.1$. The fill-out factor ff is defined here as:

$$ff = \frac{\Omega_{L_1} - \Omega}{\Omega_{L_1} - \Omega_{L_2}},$$

where Ω_{L_1} is the Roche pseudopotential at the inner critical Lagrange surface, Ω_{L_2} - analogously but in the outer critical Lagrange surface, and Ω is the pseudopotential of the system (i.e. the surface of the binary).

4.1 Averaged spot migration

We assumed the intrinsic variability in contact binaries is caused entirely by the starspot migration. We adopted a high-latitude, large spot, following our preliminary analysis (Debski et al. 2014; Debski & Żoła 2014; Debski 2020) as well as the findings in Tran et al. (2013). We recreated the lightcurve intrinsic variability by simulating longitudinally moving spot with a fixed size, temperature, and latitude. Spot position differed by 10° in subsequent lightcurves. After obtaining a full 360° longitudinal migration, we averaged all 36 lightcurves into one, Spot Migration-Averaged (SMA) lightcurve. We followed this procedure for all three base systems ($q = 0.1, 0.2, \text{ and } q = 0.3$).

Next, we performed a numerical modeling on the SMA lightcurves. The modeling was designed to not compensate for the intrinsic variability averaging. The results are presented in Table 1. The quantities in the table are relative, and should be read as a ratio of the modeled parameter value to the base (input) value, such as:

$$\Delta x \equiv \frac{x_{result}}{x_{input}},$$

where x_{input} is a value of parameter x used when simulating the base system, and x_{result} is a value of the same parameter, obtained after the numerical modeling of the SMA lightcurve of a said system. Such presentation will ease the comparison of the results between cases with different distorting agents present in simulated lightcurves.

The simulated averaged intrinsic variability has increased the apparent (obtained from modeling) inclination and mass ratio in all three cases (see Table 1). Interestingly, the increase is (almost) uniform, disregarding the mass ratio of the base system. The apparent fill-out factor has risen only for the system with the lowest mass ratio. The temperature of the secondary component remained unchanged.

4.2 Phase smearing revisited

The next run concerned the influence of the phase smearing (PS). This part is in essence an extension of the original Zola et al. (2017) study, performed on our three base systems. We introduced the phase smearing to the lightcurves, as if the systems were observed with the Kepler Long Cadence mode (0.5 h integration time). Same kind of phase smearing occurs also in the TESS mission lightcurves. The phase smearing was simulated with the assumption of six different orbital periods: $P = 0.25, 0.30, 0.35, 0.4, 0.6,$ and $P = 0.8$ d. In this run we did not simulate the intrinsic variability. During the modeling process, we did not compensate for the phase smearing.

The outcome of the numerical modeling of the phase-smear lightcurves are showed in Table 2. The results are presented, again, in relative values. In contrast to Table 1, the results in Table 2 are grouped by rows, according to the input mass ratio of the system. Columns represent different magnitudes of the phase smearing i.e. the subsequently increasing orbital periods. For example, the phase smearing causes the numerically modeled apparent inclination in the $q = 0.1$ system with orbital period adopted as $P = 0.25$ d, to be 0.88 of the original inclination in the base system (i.e. 12% lower). Under the same circumstances, the apparent mass ratio is only 0.85 of the input (true) mass ratio of the system.

As expected, the phase smearing affects the parameters the most for the shortest orbital periods. The disruption of the lightcurve causes a chain reaction of the modeled system parameters. Smoothing of the lightcurve around the secondary minimum forces the inclination to drop. This is followed by a compensation of the lightcurve amplitude, modified by the fill-out factor. The highly thinned-out lightcurve maxima are being fitted with lowering the mass ratio. Finally, because that would produce more noticeable first and fourth eclipse moments, the fill-out factor plays another role of smoothing the lightcurve in between the maxima and minima. Interestingly, because at no point the lightcurve minima change their depths with respect to each other, the temperature of the secondary component remains unchanged.

4.3 Averaged spot migration and phase smearing combined

In the final run we recreated the lightcurve distortion caused by the averaged intrinsic variability and phase smoothing simultaneously. The lightcurve preparation was similar to the one in Section 4.2, but this time the spot migration was introduced and its effect is averaged in the same fashion as in Section 4.1. The results are stored in Table 3. Just as in the last two runs, all the best fitting models we obtained, were of contact configuration ($ff > 0$).

The cumulative impact of both effects produces a very interesting image. Apart from the extremely short orbital periods, the apparent mass ratio is barely affected. This happens regardless the true mass ratio of the base system. The difference between the apparent and true mass ratio for contact binaries with orbital period of $P = 0.3$ d is just 3%. Such a difference is on the edge of the usual precision of numerical modeling. On the other hand, the decrease of the apparent mass ratio still has to be taken into account for binaries with $P < 0.3$ d.

In the simulated objects with the orbital periods $P > 0.6$ d the apparent mass ratio outgrew the input mass ratio. But as we established earlier, in the real world-scenario the intrinsic variability becomes unimportant right above $P = 0.45$ d. That means that the superposition of the PS and SMA effects will occur only below that threshold, leaving the $P > 0.45$ d objects under the influence of the PS only. This is rather fortunate, since the PS loses its impact on

the light curve quickly with a rising orbital period. The distortion of the observed mass ratio is therefore naturally diminished and remains non-negligible only for the extremely short-period contact binaries, close to $P = 0.25$ d.

The only one remaining highly affected system parameter is the fill-out factor. In the extreme cases of the lowest mass ratio and shortest orbital period, its apparent value was as much as five times larger than the input. One should remember that input fill-out factor in our simulated lightcurves was just $ff = 0.1$. In the future, a follow-up investigation should be performed for a higher value input fill-out factor.

5 THE ANALYSIS OF 47 CONTACT BINARIES

5.1 Numerical modeling scheme

To recapitulate, the primary goal of this study was to establish whether the objects in our sample are contact binaries, and to establish their photometric mass ratios. We began with rephrasing the lightcurves so that the total eclipse minimum would correspond to $\phi = 0.5$. With that we could perform a numerically uniform search with a mass ratio $q = \frac{m_2}{m_1} < 1.0$. We averaged the phased curves with a 0.005ϕ bin size. From now on we will refer to such averaged phased lightcurves simply as to the 'lightcurves'. In the next step we divided the sample into two subsets, depending on the presence of the O'Connell effect. The lightcurves with unequal brightness maxima heights, were modeled with a dark, circular starspot residing on the primary (i.e. more massive) companion. The searched spot parameters were: spot center longitude θ_s and co-latitude λ_s , and spot radius r_s . Spot relative temperature was fixed at 0.75 of the surrounding effective temperature, T_1 . The objects without the visible O'Connell effect were subdued to the spot-free lightcurve modeling. Each model had a fixed temperature of the primary component. We took the temperatures from the KEBC, as it was the most complete and uniform source at the time. If the modeling process has ended without reaching the experimentally adopted threshold or if it did not achieve convergence at all, we repeated the modeling with a third light added to the search. The resulting values of the searched parameters come from the best fitting model obtained with an MC method. For that reason they come with no formal errors. Our program did not account for the phase smearing, nor for the averaged intrinsic variability effects. The two main reasons for such course were:

- 1) the two effects are largely complementing each other in affecting the mass ratio (only four of our objects have orbital period $P \leq 0.3$ d),
- 2) it was interesting to compare our results with Zola et al. (2017), who took the phase smearing into account during the modeling process in their sample of contact binaries (hereafter referred to as Zola17 sample).

All 47 models best fitting to our lightcurves returned a contact configuration. 21 lightcurves exhibited the O'Connell effect, and therefore were modeled with a dark spot. Out of remaining 26 objects, 17 are consisting the Zola17 sample. Here we are dividing our sample into three sets, which are presented below.

5.2 Modeling results of objects with the O'Connell effect

We modeled 21 objects which needed an introduction of a starspot. 12 of them required additional third light to fit the model to data accurately. The results of the modeling are stored in Table 5. For

Table 4. Modeling result for objects coinciding with the Zola17 sample. The results from this work are flagged as row '1', while the archival results are in the row '2'. The values from this work come from the best fitting model from the MC search, hence have no formal errors. The errors for the Zola17 are presented in brackets and apply to the last significant digits. The accounting for the phase smearing introduced in Zola17 work produces almost the same result as in our work. The distinction between two approaches is more visible in the necessity of the third light introduction. However, if the third light had to be introduced in both approaches, its values are mostly similar. The temperature ratios between the two approaches are extremely similar, as predicted in Table 3. Interestingly, the fill-out factor as well do not differ in between the two approaches. A visualization of the selected relations between modeled parameters is presented in Fig. 3.

KIC #		i [°]	T_1 [K]	T_2 [K]	T_2/T_1	$\Omega_{1,2}$	$f f$ [%]	q	$L_1/(L_1+L_2)$	l_3	P_{orb} [d]
3104113	1	79.46	6535	6640	1.016	2.0514	98	0.1709	0.7988	0.0	0.8467860
	2	79.05(11)	5910	5994(1)	1.014	2.0498(4)	91	0.1666(2)	0.8027(5)	0.0	
3127873	1	87.48	6408	6164	0.962	1.9162	98	0.1088	0.8778	0.279	0.6715256
	2	90.00b	6070	5702(3)	0.939	1.9242(2)	88	0.1093(9)	0.8837(31)	0.215(2)	
5439790	1	82.96	7022	6804	0.969	2.1768	39	0.1970	0.8207	0.0	0.7960862
	2	82.69(2)	6566	6411(1)	0.976	2.1686(2)	36	0.1921(1)	0.8237(6)	0.0	
5809868	1	78.71	7208	6484	0.900	2.0535	37	0.1444	0.8851	0.0	0.4393902
	2	90.00b	6880	6365(1)	0.925	2.1743(4)	47	0.2007(2)	0.8454(11)	0.208(1)	
7698650	1	81.84	6307	6261	0.993	1.9516	74	0.1161	0.8638	0.133	0.5991551
	2	85.35(8)	6110	6082(1)	0.995	1.972(1)	70	0.1232(3)	0.8576(22)	0.159(2)	
8145477	1	84.38	6538	6284	0.961	1.9066	76	0.0988	0.8911	0.180	0.5657843
	2	90.00b	6800	6496(2)	0.955	1.922(1)	65	0.1020(3)	0.8933(33)	0.159(2)	
8265951	1	79.73	6943	6648	0.958	2.0759	53	0.1546	0.8542	0.0	0.7799575
	2	79.38(4)	7044	6780(1)	0.963	2.076(1)	38	0.1540(1)	0.8565(2)	0.0	
8539720	1	82.54	6658	6398	0.961	2.0119	90	0.1480	0.8473	0.474	0.7444991
	2	85.11(4)	6350	6119(1)	0.964	2.0378(3)	86	0.1581(2)	0.8426(19)	0.484(1)	
8804824	1	89.25	6556	6188	0.944	1.9408	75	0.1120	0.8878	0.243	0.4574038
	2	90.00b	7200	6733(2)	0.935	1.9438(6)	67	0.1109(3)	0.8937(26)	0.192(2)	
9350889	1	87.38	6996	7035	1.006	2.0127	90	0.1484	0.8251	0.236	0.725948
	2	79.92(2)	6725	6749(2)	1.004	1.9173(2)	87	0.1060(1)	0.8702(9)	0.076(1)	
9453192	1	85.11	6622	6161	0.930	2.0196	61	0.1395	0.8761	0.241	0.7188371
	2	89.51(6)	6730	6239(1)	0.927	2.054(1)	62	0.155(1)	0.8793(14)	0.269(1)	
10007533	1	83.40	6977	6379	0.914	1.8796	44	0.0824	0.9211	0.0	0.6480635
	2	90.00b	6810	6356(1)	0.933	1.9126(3)	76	0.1011(1)	0.9013(19)	0.178(1)	
10229723	1	81.50	6477	6262	0.967	2.0392	44	0.1412	0.8620	0.166	0.6287243
	2	83.16(5)	6201	6000(1)	0.968	2.057(1)	36	0.145(1)	0.8614(18)	0.166(1)	
10267044	1	79.43	7103	6901	0.972	2.1336	55	0.1865	0.8229	0.0	0.4300365
	2	89.56(7)	6808	6700(1)	0.984	2.2463(1)	55	0.240(1)	0.7828(9)	0.150(1)	
11097678	1	83.43	6493	6427	0.990	1.8858	91	0.0945	0.8807	0.267	0.9997156
	2	85.14(2)	6493	6426(1)	0.990	1.8928(1)	87	0.0967(1)	0.8792(5)	0.267(1)	
11144556	1	76.70	6803	6702	0.985	2.0273	100	0.1600	0.8219	0.381	0.6429797
	2	76.84(2)	6428	6318(1)	0.983	2.0424(2)	97	0.1607(1)	0.8246(6)	0.370(1)	
12055014	1	83.80	6448	6360	0.986	2.0362	75	0.1527	0.8362	0.124	0.4999046
	2	90.00b	6456	6439(1)	0.997	2.0606(1)	67	0.1598(1)	0.8346(9)	0.120(1)	

objects with an orbital period $P < 0.3$ d we calculated a 'corrected mass ratio', q_{corr} . This was an attempt to utilize our findings on the combined intrinsic variability averaging and phase smearing effects. q_{corr} was calculated as a two dimensional (q , P) linear interpolation based on Table 3.

5.2.1 Preferred spot longitude

In 19 out of the 21 objects the modeled cool spot resides on the trailing side of the binary. The mean longitude for such a spot is $\lambda_s = 302^\circ \pm 36^\circ$. The two remaining binaries, KIC 11618883

and KIC 8554005 have spots modeled at longitudes $\lambda_s = 94.4^\circ$ and $\lambda_s = 119.7^\circ$, respectively. Both of them have orbital periods far greater than $P = 0.45$ d cutoff ($P = 0.6848719$ d and $P = 0.6083407$ d respectively). The one system with a spot on a trailing side and the orbital period exceeding the cutoff is KIC 5290305 ($P = 0.6205088$ d). Its spot is modeled at the longitude $\lambda_s = 211.4^\circ$, which is the third lowest longitude in the set, right after the two already mentioned systems.

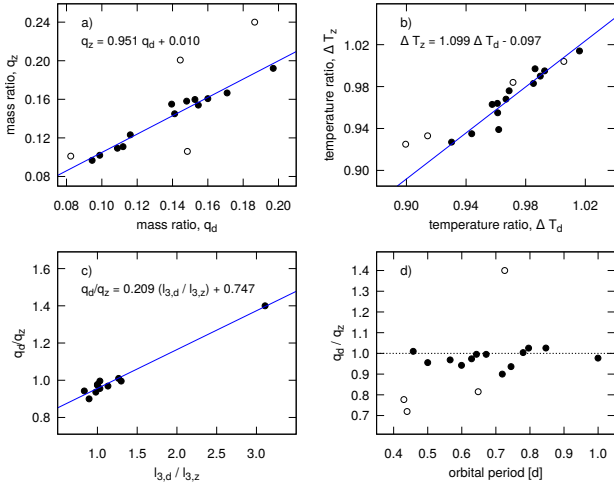


Figure 2. Relation between the modeled parameters obtained independently by Zo1a17 and in this work. Panel 'a' shown a correlation between the mass ratios and a linear fit that parametrizes the relation. The fit was made disregarding the objects for which the third light was significantly different between the methods (see the discussion). These are marked with an empty circle. Panel 'b' follows the same construct as the previous one, but depicts a correlation between the temperature ratios. Panel 'c' focuses on the relation between the ratio of mass ratios between the methods and ratio of the third light, also between the methods. Note the outlying point comes from KIC 9350889 and in this panel is not disregarded from the analysis. However, the objects for which the third light was zero in at least one method, are discarded. Panel 'd' shows the distribution of the ratio of mass ratio between methods, along the orbital period. The dotted line marks the ratio equal to one.

5.3 Reexamination of the Zo1a17 sample

The last set consists of 17 binaries studied earlier with a phase smearing taken into account. Almost all of them fall above the $P = 0.45$ d limit, and are therefore bound to have negligible intrinsic variability averaging effect. The remaining two objects are just on the inner edge of the $P = 0.45$ d limit: KIC 5809868 ($P = 0.4393902$ d) and KIC 10267044 ($P = 0.4300365$ d). These objects are also the only two with such a large difference in the relative minima depth.

The results of our modeling are superimposed with the Zo1a17 results in Table 4 and grouped per object. In addition to the effective temperatures, we are showing the temperatures ratio:

$$\Delta T = \frac{T_2}{T_1}$$

Without such an approach it would be impossible to compare our results with the archival one, since the latter used different effective temperatures for the primary component.

Most of the mass ratios obtained in this work are in agreement with those from Zo1a17. The objects in which q 's are in high disagreement are those in which there is a large discrepancy in the third light. There are four of such objects. In three of them Zo1a17 added a third light into a model, while we did not see that as a necessity. Two of them are the already mentioned KIC 5809868 and KIC 10267044. The third one is KIC 10007533, which has the lowest mass ratio in the whole set. The last object with a large third light difference is KIC 9350889. The only existing explanation for the discrepancy between the best models for this object's lightcurve is that neither our, nor the Zo1a17 models fit the descending arm of the secondary minimum very well. This overshooting of the

models might point toward a yet poorly understood fine lightcurve asymmetry worth investigating.

Not counting the four above objects, the mass ratios established with our method are highly similar to those obtained by Zo1a17. Exactly the same can be said about the temperature ratios and, surprisingly, about the fill-out factors. A depiction of the correlations between the parameters obtained with two methods presented in Fig 3. Taking into account the phase smearing during a modeling process had no influence over the best fitting models for the majority of objects in Zo1a17 sample. It might be important for objects with a significantly shorter orbital period, such as $P \approx 0.25$ d.

However, compensating solely for the phase smearing without tackling the intrinsic variability for objects below the $P = 0.45$ d limit might result in a faulty model. In Zo1a17 sample both such objects were modeled with an additional third light, which turned out to be unnecessary in our study. Moreover, we do not see any light time effect in the minima timing diagrams on either of the objects. There are also no other stars significantly close to these objects, even considering the rather large Kepler Mission pixel size. We could conclude that accounting solely for the phase smearing in case of $P < 0.45$ d binaries can be harmful to the model, but at this point we are working on just two objects. This issue is certainly interesting as it might additionally prevent an overestimation of the multiplicity of contact binaries companions.

5.4 Modeling results of the nine systems with no prevailing spot

The last set consisted of nine systems with no O'Connell effect in the averaged lightcurve. These were not included in Zola et al. (2017), hence are presented separately. Three of them are above the $P = 0.45$ d cutoff and therefore experience next to none intrinsic variability. Remaining six objects show moderate and heavy intrinsic variability which largely averages itself out. The resulting best fit model parameters are given in Table 6. Five out of nine objects needed an introduction of a third light.

5.5 Contact binaries with a companion

28 out of 47 contact binaries in this study needed a third light introduced to the model. Four of them are most probably due to the pixel light contamination. Two of such, KIC 2437038 and KIC 2570289 are located in a dense field of NGC 6791. The next two, KIC 11097678 and KIC 11618883 have considerably bright companions, which could not be resolved with the large Kepler Mission pixel size. None of the four binaries show any light-time effect in their minima timing.

In contrast, we found that KIC 8265951 has a considerable light-time effect in the minima timing, but its best fitting model shows no third light. Two other objects: KIC 10528299 and KIC 7709086 are also modeled with no third light, but their minima timing diagrams show a possible light time effect.

There are additionally three binaries with some possibility of the pixel contamination by a nearby source: KIC 3127873, KIC 8432859, and KIC 8842170. These objects have also no visible light-time effect. Assuming they are indeed contaminated, the lower limit for a fraction of binaries with a possible companion is 53%. If we count in the three uncertain objects, then the fraction rises to 60%. These limits fall close to the estimates made by Pribulla & Rucinski (2006). In their work the estimated fraction of contact binaries with a companion was about 59% with a lower limit of about 40%.

Table 5. Modeling results for objects with a visible O’Connell effect. The light curves of objects in this set were modeled with a cool spot on a surface of a primary component. The temperature of a spot was fixed to $T_s = 0.75 T_1$ and therefore is not included in this table. The primary component effective temperature was the only fixed parameter, per the normal use of W-D code. The q_{corr} are the modeled mass ratios of the objects with $P < 0.3$ d.

KIC #	i [°]	T_1 [K]	T_2 [K]	$\Omega_{1,2}$	$f f$	q	q_{corr}	$L_1/(L_1+L_2)$	l_3	θ_s [°]	λ_s [°]	r_s [°]	P_{orb} [d]
2159783	79.9	6140	6326	2.0246	69%	0.1449	-	0.81888	0.0	15.5	335.5	18.6	0.3738842
2437038	82.7	5461	5944	2.0743	84%	0.1747	0.1876	0.74920	0.43972	69.1	291.9	11.6	0.2676785
2570289	86.6	6360	6470	1.9341	92%	0.1143	0.1210	0.84953	0.69571	74.3	330.2	10.0	0.2790278
3342425	87.8	6306	6463	1.9059	100%	0.1050	-	0.85232	0.10044	40.9	293.0	10.8	0.3934148
4036687	82.4	6200	6378	1.9813	96%	0.1368	0.1410	0.81960	0.27032	15.2	329.5	16.3	0.2997993
4244929	85.8	5976	6047	1.9966	100%	0.1454	-	0.81934	0.53333	9.6	231.5	21.8	0.3414027
5283839	86.5	6239	6534	1.9541	92%	0.1231	-	0.82568	0.21885	40.1	299.0	10.9	0.3152311
5290305	81.6	6542	6186	2.2019	41%	0.2097	-	0.82872	0.17448	32.9	211.0	14.4	0.6205088
6118779	78.4	5715	6003	1.9133	93%	0.1060	-	0.84010	0.0	26.9	341.4	13.7	0.3642464
7821450	81.4	5155	5513	2.1741	38%	0.1954	-	0.75538	0.31482	28.8	294.9	10.4	0.3147619
8143757	79.9	5454	5592	2.2874	23%	0.2368	-	0.76450	0.0	9.1	265.1	15.3	0.3565228
8432859	84.8	6352	6537	1.9557	92%	0.1238	-	0.83488	0.20001	19.9	323.2	15.8	0.3511705
8554005	83.3	7298	7302	2.4560	59%	0.3557	-	0.70466	0.18044	39.9	119.8	10.0	0.6083407
8682849	78.9	5631	5831	1.9579	80%	0.1206	-	0.83667	0.0	21.2	346.3	15.7	0.3525548
8842170	79.2	5589	5835	1.9812	96%	0.1367	-	0.81036	0.38752	10.2	295.9	22.5	0.3493917
9087918	80.2	6085	6163	2.3056	31%	0.2511	-	0.76249	0.0	6.0	304.5	21.6	0.4456069
9283826	80.0	5987	6498	2.0724	70%	0.1666	-	0.76701	0.0	9.2	300.4	23.1	0.3565238
10322582	75.5	5863	6530	1.9733	78%	0.1265	0.1318	0.78822	0.0	23.3	328.2	21.1	0.2912692
10528299	80.9	6302	6630	2.1783	42%	0.1998	-	0.77201	0.0	10.2	271.6	21.3	0.3998018
10618253	84.2	6580	6580	1.9415	85%	0.1155	-	0.85852	0.0	17.2	339.8	15.2	0.4374028
11618883	87.6	4347	4403	2.1801	80%	0.2251	-	0.75900	0.58369	10.0	93.6	25.8	0.6848719

Table 6. The results of a light curve modeling for objects in which the averaged phase curve did not showed any O’Connell effect. The primary component temperature was a fixed parameter during the modeling process.

KIC #	i [°]	T_1 [K]	T_2 [K]	$\Omega_{1,2}$	$f f$	q	$L_1/(L_1+L_2)$	l_3	P_{orb} [d]
7601767	77.4	6567	6388	2.1083	23%	0.1610	0.8484	0.2463	0.5991551
7709086	75.7	6108	6290	2.1593	37%	0.1886	0.7930	0.0	0.4094746
8496820	82.5	6601	6558	2.0795	76%	0.1727	0.8169	0.0	0.4369669
9030509	87.2	5326	5393	2.0581	100%	0.1756	0.7927	0.2960	0.4017846
9151972	87.7	5622	5716	2.0407	100%	0.1668	0.7982	0.5448	0.3867961
9703626	76.6	6060	6088	2.2135	36%	0.2120	0.7927	0.0	0.4151477
9776718	81.3	7205	7277	2.0325	86%	0.1560	0.8177	0.0	0.5443510
10395609	87.2	6566	6564	2.0434	99%	0.1675	0.8096	0.2114	0.3642540
12352712	89.4	6667	6469	1.8900	87%	0.0952	0.8877	0.2094	0.7220650

5.6 The Period-Mass relation

In addition to the numerical modeling, we explored the physical properties of our binaries. We started with calculation of the masses of the components using the [Gazetas & Stępień \(2008\)](#) relations. We found that they produce mass ratios largely different from our photometric q ’s. The differences were easily reaching as much as 100%. We dealt with this problem by refining the relation for secondary components. This choice was dictated by a rather low correlation coefficient in the Period-Secondary Component Mass relation in their work. We therefore calculated the primary component masses in our sample using the original formula:

$$\log(m_1) = (0.755 \pm 0.059)\log(P) + 0.416 \pm 0.024, \quad (1)$$

and then applied our photometric mass ratios to obtain the secondary component masses. Finally, we fitted them with a log-log function. The resulting improved Period-Secondary Component Mass relation is:

$$\log(m_2)_{[low\ q]} = (0.6907 \pm 0.1483)\log(P) - 0.4049 \pm 0.0437, \quad (2)$$

The discrepancy between the original relation and our solution is

most probably due to the under-representation of the low- q binaries in the [Gazetas & Stępień \(2008\)](#) work. We treat our solution as complementary to theirs, but in a low- q regime. The calculated masses are shown in Table 7.

5.7 Distance calculation

In the next step we calculated the distances to our objects, starting with the distance modulus method. First, we transformed their brightness in g, r, i filters ([Brown et al. 2011](#)) into (B-V) colors and V magnitudes in Johnson system using [Jester et al. \(2005\)](#) formulas. The absolute magnitudes in V filter were calculated using the [Rucinski \(2004\)](#) relation. Then, the interstellar extinction was found with the [Schlafly & Finkbeiner \(2011\)](#) extinction maps available at the NASA/IPAC Infrared Science Archive⁴. We assumed the color excess follows the $A_V = 3.1 E(B - V)$ relation.

⁴ <https://irsa.ipac.caltech.edu/applications/DUST/>, accessed in November 2020

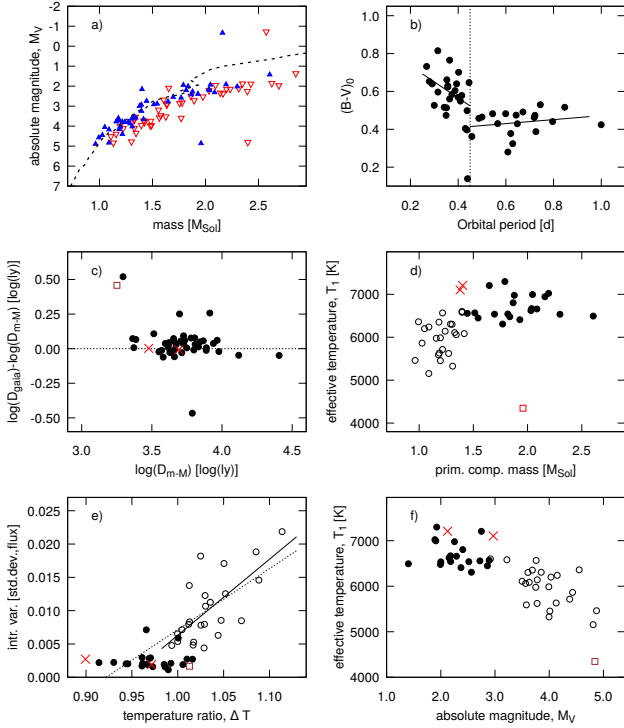


Figure 3. Relations between the observed and calculated parameters. Panel a) shows the Mass - Absolute Magnitude relation for the total mass of a binary (empty triangles), and the primary star mass only (filled triangles). The dashed line shows the relation for single Main Sequence stars. Panel b) shows the Period-Color relation. The otherwise logarithmic Eggen (1967) relation can be successfully expressed as two linear relations, divided by the $P = 0.45$ d cut-off. Panel c) compares the distance modulus distances (D_{m-M}) with the distances calculated via the parallax (D_{gaia}). The red X-marks are the KIC 10267044 and KIC 5809868 systems. The brown square is the KIC 11618883. The remaining systems are shown as the black filled circles. Panel d) depicts the relation between the primary component mass and its effective temperature. Objects in binaries with $P < 0.45$ are shown with empty circles, and the X-marks and empty square denote the same systems as in previous panel. Panel e) shows the relation between the intrinsic variability and the modeled temperature ratio of the binary. The scheme of the symbols is as in the previous panel. The dashed line is the linear fit to the $P < 0.45$ systems; the solid line represent the same fit, but excluding the KIC 10267044 and KIC 5809868 systems. Panel f) shows the relation between the primary star effective temperature and the absolute magnitude of the system. Symbol scheme is as in the previous panel. The whole right row of this Figure presents Period-Color relation or its variations.

Because KIC 8265951 clearly stands out from the rest ($M_V = -0.69$ with $m_1 + m_2 = 2.57 M_{Sol}$), we decided to verify all distances using the Gaia mission parallaxes (Lindgren et al. 2021). We adopted the DR3⁵ data and applied the mean offset for W UMa-type contact binaries (Ren et al. 2021). The resulting distances are presented in Table 8. We compared the distance modulus- and parallax-based distances and found them to be very consistent (correlation coefficient $r = 0.9097$, see panel c) in Fig. 3). The distance to KIC 8265951 was confirmed, which means that the system is located indeed on the outskirts of the dusty region Sh2-109.

The differences in the distances obtained with two methods are

Table 7. Calculated masses of the binary components. The masses of primaries were calculated with the Gazeas & Stępień (2008) formula. The masses of secondaries were obtained by multiplying the primary masses by the photometric mass ratios established in this work.

KIC #	m_1	m_2	KIC #	m_1	m_2
2159783	1.240	0.180	8682849	1.186	0.143
2437038	0.963	0.168	8804824	1.444	0.162
2570289	0.994	0.114	8842170	1.178	0.161
3104113	2.299	0.393	9030509	1.309	0.181
3127873	1.929	0.210	9087918	1.416	0.355
3342425	1.289	0.135	9151972	1.272	0.212
4036687	1.050	0.144	9283826	1.196	0.199
4244929	1.158	0.168	9350889	2.046	0.304
5283839	1.090	0.134	9453192	2.031	0.283
5290305	1.818	0.381	9703626	1.342	0.284
5439790	2.194	0.432	9776718	1.647	0.246
5809868	1.401	0.252	10007533	1.878	0.155
6118779	1.216	0.129	10229723	1.836	0.259
7601767	1.513	0.243	10267044	1.378	0.257
7698650	1.770	0.206	10322582	1.027	0.130
7709086	1.328	0.250	10395609	1.216	0.202
7821450	1.089	0.213	10528299	1.304	0.261
8143757	1.196	0.284	10618253	1.396	0.161
8145477	1.695	0.167	11097678	2.606	0.246
8265951	2.160	0.413	11144556	1.867	0.299
8432859	1.183	0.146	11618883	1.958	0.441
8496820	1.395	0.241	12055014	1.544	0.236
8539720	2.086	0.309	12352712	2.038	0.195
8554005	1.791	0.637			

shown in the Panel c) of Fig. 3. There are five objects with rather large distance discrepancies. First one, KIC 11618883, is marked as an empty square in the Figure 3. This is a system with the by far lowest effective temperature and the greatest (B-V) color. It has a barely resolved, white companion star. It is highly probable, that the companion star is in fact the W UMa binary, while the red star is just a foreground object. We will verify this in another study. The second binary, KIC 9151972, has a D_{m-M} distance overshoot, which is caused most probably by the high third light contamination. We did not take the third light into account in any of the binaries, when calculating the distance modulus. The decision was dictated by the unknown impact of the companion color on the (B-V) of the system. The next two binaries, KIC 9283826 and KIC 2437038, stand out with their ΔT ratios, having a secondary star of a significantly greater apparent effective temperature than the primary. Their color might be under a large influence of their spot activity. It is possible that systems going through such an evolutionary stage might not follow the known Period-Color relation very well. It should be noted though that those two binaries are not deviating from the Period-Color relation seen in Panel b) of the same Figure. Moreover, there is one system with an even greater temperature ratio: KIC 10322582. The latter binary is not experiencing distance discrepancy. Nevertheless, because its total eclipse is rather dubious, it might be the case that its inclination is in fact lower, the mass ratio greater and the resulting temperature ratio much closer to $\Delta T = 1$. Such possibility should be investigated in the next study. The last binary with a large distance difference is KIC 9776718. This system has a calculated color index (B-V)=0.61, although in the DSS maps it appears to have a very white color. We assume it is probable that the SDSS magnitudes we used for the (B-V) calculation might be flawed.

⁵ <https://gea.esac.esa.int/archive/>, accessed in June 2021

5.8 The Mass-Absolute Magnitude relation

Contact binaries are known to be about one magnitude less bright than solo main sequence stars of the same mass (Rucinski 2004). It is due to the more massive component being the primary source of energy that is being shared across the common envelope. We have shown in panel a) of Fig. 3 that this relation holds also in our dataset (total mass of a binary is represented by the empty triangles in the plot). At the same time, despite the shared energy, the primary components follow the Mass-Absolute Magnitude relation to the point of reaching $m_1 \approx 1.9M_\odot$ (filled triangles in the plot). The absolute magnitude here is the total brightness of the binary. The Mass-Absolute Magnitude relation for the solo main sequence stars is taken from the Pecaut & Mamajek (2013) updated by E.E.Mamajek⁶.

5.9 The Period-Color relation

Encouraged by the above findings we constructed the Period-Color (PC) diagram for our sample. The relation is depicted in panel b) of Fig. 3. A traditional way of looking at the diagram is via the logarithmic relation. We propose to look at the diagram through the lens of the $P = 0.45$ d limit. When doing so, two linear relations became apparent, instead of one logarithmic. Hence, the PC relation for $P < 0.45$ d binaries is:

$$(B - V)_0 = 0.905 (\pm 0.138) - 0.847 (\pm 0.374)P. \quad (3)$$

It must be noted that the correlation coefficient for this relation is rather weak: $r \approx 0.43$. For the $P > 0.45$ d binaries the PC relation is:

$$(B - V)_0 = 0.367 (\pm 0.078) + 0.105 (\pm 0.116)P, \quad (4)$$

with an even weaker correlation coefficient $r \approx 0.21$. Our sample contains objects with mass ratios mostly below $q < 0.25$, therefore the double PC relation might not necessarily work in mass ratios above that limit.

Panel d) of the Fig. 3 presents a variation of the PC relation. The Mass - Effective Temperature for the Primary Star relation makes it easier to see the two sub-populations of objects. Both sub-populations form clumps with no apparent trends. The effective temperatures come from the Kepler Input Catalog, and therefore have a rather large uncertainty (on average 400 K).

Panel f) of the Fig. 3 show another version of the PC relation. In the System Absolute Magnitude - Primary Star Effective Temperature relation the two sub-populations are more separated, and therefore better visible. In both panels d) and f) we marked the KIC 10267044 and KIC 5809868 systems ($P < 0.45$ d) with X-marks and the KIC 11618883 ($P > 0.45$ d) with the empty square.

5.10 The relation between the Apparent Temperature Ratio and the Light Curve Intrinsic Variability

The only parameter that we successfully tied to the magnitude of the light curve intrinsic variability is the apparent temperature ratio of a binary. The binaries with $P < 0.45$ d follow a weak trend of light curve intrinsic variability in a correlation with the apparent temperature ratio, $\Delta T = T_2/T_1$. The relation is shown in the Panel e) in Figure 3 (the $P < 0.45$ d binaries are depicted with the empty

circles). If we neglect the KIC 10267044 and KIC 5809868 binaries (marked with X), then the relation is: $I_{intr}V_{ar} = 0.1142\Delta T - 0.1079$ with the correlation coefficient $r = 0.6971$. The $I_{intr}V_{ar}$ is the magnitude of the light curve intrinsic variability as measured in Section 4. If the two neglected binaries were to be taken into account, then the slope of the correlation would be $a = 0.0915$ with the correlation coefficient $r = 0.7162$.

6 CONCLUSIONS

The effect of averaged lightcurve intrinsic variability

This work explored the impact of the averaged lightcurve intrinsic variability in contact binaries on the results of the light curve numerical modeling. We simulated the effect in low- q contact binaries by averaging the synthetic longitudinal spot migration. We found that the intrinsic variability averaging leads to an increase of the apparent (i.e. resulting from the modeling) mass ratio. The apparent increase of $\Delta q = 5\%$ was independent of the input mass ratio. We observe an increase of the apparent inclination and the apparent fill-out factor; for the latter parameter the increase occurs only for the lowest input mass ratio. The effective temperature of the secondary component remains unaffected.

The averaged intrinsic variability largely cancels itself out with the Kepler- and TESS-like phase smearing effect. When the two effects are taken into account, the apparent mass ratio is virtually unaffected for systems with an orbital period of $P \geq 0.35$ d, while for systems with $P = 0.3$ d the apparent mass ratio is decreased by 3% with respect to the input. The apparent mass ratio decrease was at non-negligible 9% level for systems with a very short orbital period of $P = 0.25$ d. Both lightcurve-distorting effects strongly increase the apparent fill-out factor. The secondary component effective temperature remains unchanged in all cases.

Numerical modeling results

We performed a lightcurve modeling of 47 totally eclipsing binaries from the KEBC database, mainly in search of the photometric mass ratio and the confirmation of their contact nature. We did not take into account the phase smearing nor the intrinsic variability averaging, because for majority of our objects these two effects neutralize each other in the mass ratio domain. Our modeling returned a contact configuration for all 47 systems. 21 of our objects were exhibiting the O'Connell effect in the phased and averaged 4-years-long lightcurve. 19 of them have a primary brightness maximum lower than the secondary. This can be interpreted as a dark region located on the trailing side of the binary. Numerical modeling returned an average longitude of such a long-lasting dark region to be $\lambda = 302^\circ$ ($\sigma = 36^\circ$).

Next 17 objects in our sample were studied earlier by Zola et al. (2017), who took the phase smearing into account during the modeling. These objects have orbital periods $P > 0.4$ d. Our modeling returned a very similar mass ratios and temperature ratios to the previous study. Any deviations between our and their results bear no relation with the orbital period. In contrast to the previous study, we found it was not necessary to introduce a third light in three of the studied systems. This inclines us to conclude that taking the phase smearing into account during the numerical modeling of contact binaries with such a long orbital periods is unnecessary.

We resolved that out of 47 objects in our sample, no less than 53% have a possible third companion. Three objects have a possible

⁶ https://www.pas.rochester.edu/~emamajek/EEM_dwarf_UBVIJHK_colors_Teff.txt, version 2021.03.02

Table 8. Calculated parameters of contact binaries in our sample. The B-V colors and V magnitudes were calculated with the Jester et al. (2005) formula from the SDSS magnitudes. The interstellar extinction A_V come from the Schlafly & Finkbeiner (2011) reddening maps. The absolute magnitudes in V filter were calculated with Rucinski (2004) formula. The D [ly] distances were calculated with the standard distance modulus method. The D_{Gaia} [ly] distanced were calculated from Gaia parallaxes for a verification.

KIC #	B-V	V	A_V	M_V	D [ly]	D_{Gaia} [ly]	KIC #	B-V	V	A_V	M_V	D [ly]	D_{Gaia} [ly]
2159783	0.77	15.14	0.57	3.78	4711	5039^{+160}_{-150}	8682849	0.77	15.90	0.34	4.13	6300	6147^{+347}_{-312}
2437038	0.87	16.21	0.42	4.87	4980	8816^{+2015}_{-1383}	8804824	0.41	14.74	0.14	2.72	7742	7817^{+370}_{-338}
2570289	0.78	15.53	0.41	4.55	4250	3989^{+451}_{-368}	8842170	0.83	15.08	1.09	3.58	3939	4294^{+111}_{-105}
3104113	0.68	13.57	0.50	2.00	5319	6566^{+156}_{-149}	9030509	0.87	14.70	0.52	4.00	3549	3373^{+343}_{-285}
3127873	0.68	15.29	0.60	2.37	9499	8999^{+542}_{-484}	9087918	0.74	14.64	0.30	3.63	4518	5336^{+153}_{-145}
3342425	0.73	15.24	0.29	3.85	5414	6185^{+267}_{-246}	9151972	0.73	15.54	0.39	3.78	6140	2104^{+17}_{-16}
4036687	0.63	15.37	0.33	4.03	5167	4827^{+156}_{-147}	9283826	0.72	13.20	0.30	3.99	1971	6510^{+158}_{-151}
4244929	0.65	15.21	0.40	3.75	5310	5736^{+221}_{-205}	9350889	0.52	13.64	0.40	1.91	6010	7145^{+209}_{-197}
5283839	0.74	15.30	0.44	4.15	4519	5149^{+188}_{-175}	9453192	0.51	14.06	0.14	2.15	7357	8337^{+555}_{-490}
5290305	0.59	14.39	0.65	2.18	6681	6973^{+228}_{-214}	9703626	0.65	15.64	0.21	3.56	7716	7472^{+841}_{-687}
5439790	0.52	13.32	0.26	1.89	5609	5673^{+104}_{-100}	9776718	0.61	15.14	0.39	2.75	8184	14586^{+2087}_{-1623}
5809868	0.47	12.99	1.04	2.13	3008	3029^{+29}_{-28}	10007533	0.49	13.91	0.18	2.25	6432	6876^{+167}_{-159}
6118779	0.85	15.69	0.25	4.38	5314	5764^{+250}_{-230}	10229723	0.55	12.04	0.69	1.99	2432	2838^{+36}_{-35}
7601767	0.54	14.60	0.25	2.89	6381	7605^{+2924}_{-1653}	10267044	0.47	14.07	0.21	2.97	4923	4836^{+89}_{-85}
7698650	0.66	15.37	0.54	2.56	9238	10532^{+775}_{-676}	10322582	0.69	14.94	0.17	4.43	3808	3313^{+57}_{-55}
7709086	0.82	15.99	0.85	3.50	6965	7758^{+465}_{-415}	10395609	0.62	14.63	0.18	3.76	4467	4173^{+75}_{-72}
7821450	0.93	15.15	0.34	4.81	3266	4185^{+186}_{-171}	10528299	0.63	14.07	0.18	3.61	3710	3608^{+47}_{-46}
8143757	0.68	14.90	0.15	4.01	4590	4525^{+207}_{-190}	10618253	0.64	12.92	0.45	3.22	2309	2735^{+30}_{-29}
8145477	0.49	14.83	0.18	2.52	8686	9397^{+473}_{-430}	11097678	0.53	13.33	0.33	1.40	6802	6982^{+174}_{-166}
8265951	0.45	12.76	2.71	-0.69	4580	4007^{+51}_{-50}	11144556	0.56	13.62	0.25	2.40	5082	5754^{+104}_{-101}
8432859	0.67	17.20	0.48	3.69	13156	11667^{+2614}_{-1805}	11618883	1.41	13.80	0.27	4.84	1783	5110^{+82}_{-79}
8496820	0.55	12.67	0.47	2.91	2353	2398^{+16}_{-16}	12055014	0.53	13.58	0.19	2.86	4168	4466^{+65}_{-63}
8539720	0.58	12.99	0.16	2.29	4181	4616^{+78}_{-76}	12352712	0.54	16.86	0.22	2.18	25526	22215^{+705}_{-4549}
8554005	0.37	12.73	0.29	1.92	4134	4211^{+73}_{-71}							

companion seen in the minima timing diagram, but their best fitting models show no third light.

We established that the distances to our objects calculated with the Rucinski (2004) formula are in general in a good agreement with the Gaia DR3 corrected parallaxes.

We refined the Orbital Period - Secondary Component Mass relation from Gazeas & Stepień (2008) to work with low- q contact binaries.

We resolved to not calculate the radii of the components of our binaries since the ff parameter is heavily affected by both the intrinsic variability averaging and the phase smearing effects. The resulting radii would be highly questionable.

Recently, Li et al. (2020) published a study of 380 Kepler contact binaries, which partially includes our 47-object sample. Unfortunately, because of the parameter determination in their work we concluded that it is hardly possible to reliably compare our findings.

The $P = 0.45$ d cutoff

Upon the examination of the magnitude of the intrinsic variability as a function of the orbital period, we found a sharp cutoff at $P = 0.45$ d. The lightcurves of objects above this limit show next to none measurable intrinsic variability. Below the cutoff the lightcurves immediately start to experience a severe intrinsic variability of various intensities. This means that the intrinsic averaging effect will not be present in contact binaries with orbital period $P > 0.45$ d.

Following this cutoff, we found that the Orbital Period - Color relation can be expressed as two linear relations, instead of a logarithmic one. As a variant to this relation, we showed that the primary component Mass - Effective Temperature is populated by two distinct groups of objects, distinguished by the $P = 0.45$ d cutoff only.

Most of the above observations coincide with the characteristics of the A- and W-subtypes of the W UMa-type contact binaries. The division itself became questionable in recent years, as more and

more contact binaries were shown to switch in between the subtypes in rather short timescales. Our Period - Intrinsic Variability diagram (left panel in Fig. 1) provides a new perspective on the issue. Since the starspot-based intrinsic variability can distort all parts of the lightcurve, it is natural to expect that the $P < 0.45$ d binaries will be able to change their relative minima depths. Following this, the $P < 0.45$ d binaries can be either W- or A-subtype, depending on the moment of observations. On the other hand, the $P > 0.45$ d binaries remain always in the A-subtype. In this picture the division based on the relative minima depth is not reliable in the morphological sense. In our opinion the A/W-subtype division, if it is to stay, should remain in the purely phenomenological realm, i.e. as a description of a transient lightcurve, not the object itself.

We infer that a proper distinction between the contact binary types should be based on the $P = 0.45$ d cutoff only. Granted, we expect this boundary might be violated to some extent by objects with a low enough inclination, but this would be the result of the projection effects of high-latitude, lightcurve-disturbing phenomena on the surface of the binary (see Debski 2020, for a short introduction to the topic). A study of this phenomenon, along with the further investigation of the $P = 0.45$ d intrinsic variability boundary, should be presented in an upcoming paper, as it is far out of the scope of this work. At this point, we expect that the (partially) synchronous rotation reaches a critical velocity at the orbital period cutoff. With a shorter orbital period, the rotation causes the magnetic dynamo to cross an innate threshold and unbind itself. That would result in an immediate formation of large starspots occurring near the polar regions, just as it is in case of fast rotating solo stars. Such scenario opens an interesting path toward studying the interiors of contact binaries.

Light curve intrinsic variability and the spot activity

The objects with $P < 0.45$ d showed a wide range of intrinsic variability, while our simulations (Section 4) were performed for a fixed-size starspot. Because of that, our simulations may not represent the situation occurring in all objects equally well. It would be best to estimate the influence of the light curve intrinsic variability averaging with some independent parameter. Unfortunately, the intensity of the intrinsic variability below $P = 0.45$ d is not correlated with the orbital period, effective temperature, nor the photometric color. The only parameter correlating with the intrinsic variability seems to be the apparent temperature ratio, ΔT . It would be advisable to estimate a possible increase of the Δq basing on the ΔT .

Up to this point we only assumed that the apparent $T_2 > T_1$ is a numerical artifact caused by the simplistic model, rather than a real temperature ratio. In this scenario, the apparent $T_2 > T_1$ is induced by a presence of large, cool starspots on the surface of the primary star. The correlation of the apparent ΔT with the light curve intrinsic variability proves that the $T_2 > T_1$ is tied to the starspot activity. Moreover, such effect would be magnified with a dark 'spot' residing very close or around the neck of the binary, on the primary component. Our findings about the 'long-prevailing spot' close to the binary neck (Section 5.2.1) seems to back up such a possibility. On the other hand, the simulated light curve intrinsic variability (Section 4) showed that the effect of averaging does not change the T_2 . If the effect itself does not influence the ΔT , then it acts as an indicator of the overall 'spottiness' (the total spot coverage) of the primary component. The increased spot coverage on the primary would be therefore the main cause of the elevated levels of the apparent T_2 .

The impact on the current and planned photometric missions

We see that the results obtained in this work can be useful when studying contact binaries observed with a range a different surveys. The photometry from the Kepler, as well as TESS space telescopes, is expected to be burdened with both phase smearing and intrinsic variability averaging effects. On the other hand, the LSST and GAIA lightcurves, because of their short exposure times and long-time base, will result with no phase smearing and a rather significant intrinsic variability averaging effect. We expect the same effect to be of importance in the small telescope photometric surveys, such as SuperWASP, CRTS, LINEAR and many other.

ACKNOWLEDGEMENTS

The case study of every object was done largely via the Simbad⁷ database (Wenger et al. 2000) and the Aladin software (Bonnarel et al. 2000; Boch & Fernique 2014).

The Author gratefully acknowledges the financial support for this work given by the Polish Ministry of Science and Higher Education under the Preludium 12 Grant no. 2016/23/N/ST9/01218. The Author would like to thank to his friends who made this work possible to finish, either by proofreading or by giving a moral support during last two exceptionally tough years.

7 DATA AVAILABILITY

The data underlying this article will be shared on reasonable request to the corresponding author. Some of the contact binary helpful formulas were integrated as free to use calculators on our project's webpage⁸.

REFERENCES

- Binnendijk L., 1965, Veroeffentlichungen der Reimeis-Sternwarte zu Bamberg, 27, 36
- Boch T., Fernique P., 2014, in Manset N., Forshay P., eds, Astronomical Society of the Pacific Conference Series Vol. 485, Astronomical Data Analysis Software and Systems XXIII. p. 277
- Bonnarel F., et al., 2000, *A&AS*, 143, 33
- Borucki W. J., et al., 2010, *Science*, 327, 977
- Brown T. M., Latham D. W., Everett M. E., Esquerdo G. A., 2011, *AJ*, 142, 112
- Claret A., Bloemen S., 2011, *A&A*, 529, A75
- Claret A., Hauschildt P. H., Witte S., 2013, *A&A*, 552, A16
- Debski B., 2019, *CoSka*, 49, 258
- Debski B., 2020, *Contributions of the Astronomical Observatory Skalnaté Pleso*, 50, 490
- Debski B., Zola S., 2014, in Binary Systems, their Evolution and Environments. pp P4–2
- Debski B., Baran A., Zola S., 2014, *Contributions of the Astronomical Observatory Skalnaté Pleso*, 43, 427
- Debski B., Zola S., Baran A., 2015, *CoSka*, 496, 293
- Eggen O. J., 1967, *Mem. RAS*, 70, 111
- Flannery B. P., 1976, *ApJ*, 205, 217
- Gazeas K., Stępień K., 2008, *MNRAS*, 390, 1577
- Jester S., et al., 2005, *AJ*, 130, 873
- Kopal Z., 1959, *Close binary systems*. London: Chapman & Hall
- Li X.-Z., Liu L., Zhu L.-Y., 2020, *PASJ*, 72, 103

⁷ <http://simbad.u-strasbg.fr/>

⁸ <http://bade.space/soft/>

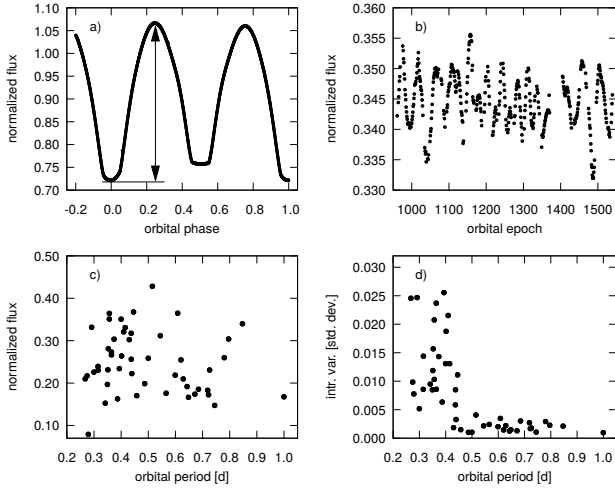


Figure A1. A visualization of an alternative method of the intrinsic variability quantification and measurement. For details see description in Appendix A

- Lindgren L., et al., 2021, *A&A*, 649, A4
 Lucy L. B., 1968a, *ApJ*, 151, 1123
 Lucy L. B., 1968b, *ApJ*, 153, 877
 Lucy L. B., 1976, *ApJ*, 205, 208
 Matijević G., Prša A., Orosz J. A., Welsh W. F., Bloemen S., Barclay T., 2012, *AJ*, 143, 123
 Mullan D. J., 1975, *ApJ*, 198, 563
 Pecaut M. J., Mamajek E. E., 2013, *ApJS*, 208, 9
 Pribulla T., Rucinski S. M., 2006, *AJ*, 131, 2986
 Prša A., et al., 2011, *AJ*, 141, 83
 Ren F., Chen X., Zhang H., de Grijs R., Deng L., Huang Y., 2021, *ApJ*, 911, L20
 Rucinski S. M., 2004, *New Astron. Rev.*, 48, 703
 Samec R., Caton D., Robb R., Faulkner D. R., 2018, *Research Notes of the American Astronomical Society*, 2, 13
 Schlafly E. F., Finkbeiner D. P., 2011, *ApJ*, 737, 103
 Terrell D., Wilson R. E., 2005, *Ap&SS*, 296, 221
 Tran K., Levine A., Rappaport S., Borkovits T., Csizmadia S., Kalomeni B., 2013, *ApJ*, 774, 81
 Webbink R. F., 2003, *Contact Binaries*. ASPC, p. 76
 Wenger M., et al., 2000, *A&AS*, 143, 9
 Wilson R. E., 1979, *ApJ*, 234, 1054
 Wilson R. E., Devinney E. J., 1971, *ApJ*, 166, 605
 Zola S., Gazeas K., Kreiner J. M., Ogloza W., Siwak M., Koziel-Wierzbowska D., Winiarski M., 2010, *MNRAS*, 408, 464
 Zola S., Baran A., Debski B., Jableka D., 2017, *MNRAS*, 466, 2488

APPENDIX A: MEASUREMENT OF THE INTRINSIC VARIATION

In the main body of this work we adopted linear ephemeris for the phase-folding process. This choice is susceptible to the variability of the orbital period (real or apparent). Such variability can introduce an additional scatter of the phase-folded lightcurve. This period variation-caused scatter can easily be confused with the noise coming from the stellar intrinsic variability. It is especially visible in the left panel of Fig. 1, where one datapoint at $P = 0.6$ d stands out. This measurement comes from KIC 8265951, which minima timing diagram shows clearly a strong light-time effect.

To confirm the $P = 0.45$ d sharp cutoff we measured the intrinsic variability in our sample with a range of alternative methods. One of such is based on a measurement of the standard deviation of the range between the height of the primary brightness maximum and the primary minimum. In the Figure A1, Panel a) depicts the measured lightcurve amplitude, and Panel b) shows the variation of the amplitude in terms of orbital epochs. Panel c) shows that there is no correlation between the mean amplitude of the lightcurve and the orbital period. Such correlation could influence the intrinsic variability vs orbital period relation measured with this particular method. The final results are shown in the Panel d) of Fig. A1. This diagram is very similar to the aforementioned Panel a) of Fig. 1, but this time the previously outlying datapoint from KIC 8265951 is nicely following other $P > 0.45$ d systems.

We reproduced the same sharp cut-off at $P = 0.45$ d with every method we used. In the main body of this work we chose to show the relation between the intrinsic variability and orbital period with the standard deviation of the phase-folded curve noise because this representation was the most straightforward. Other methods need explanation that is out of scope of this article and will be presented elsewhere.

APPENDIX B: THE LIGHTCURVES AND THE BEST FITTING MODELS

Figures B1 to B3 contain phased and averaged lightcurves of the 47 studied objects. The light curves are shown as empty circles. The best-fitting models are superimposed over the lightcurves as a continuous line. Each panel is described by the KIC number of the given object's light curve. The light curves are presented in the units of the normalized flux.

This paper has been typeset from a $\text{\TeX}/\text{\LaTeX}$ file prepared by the author.

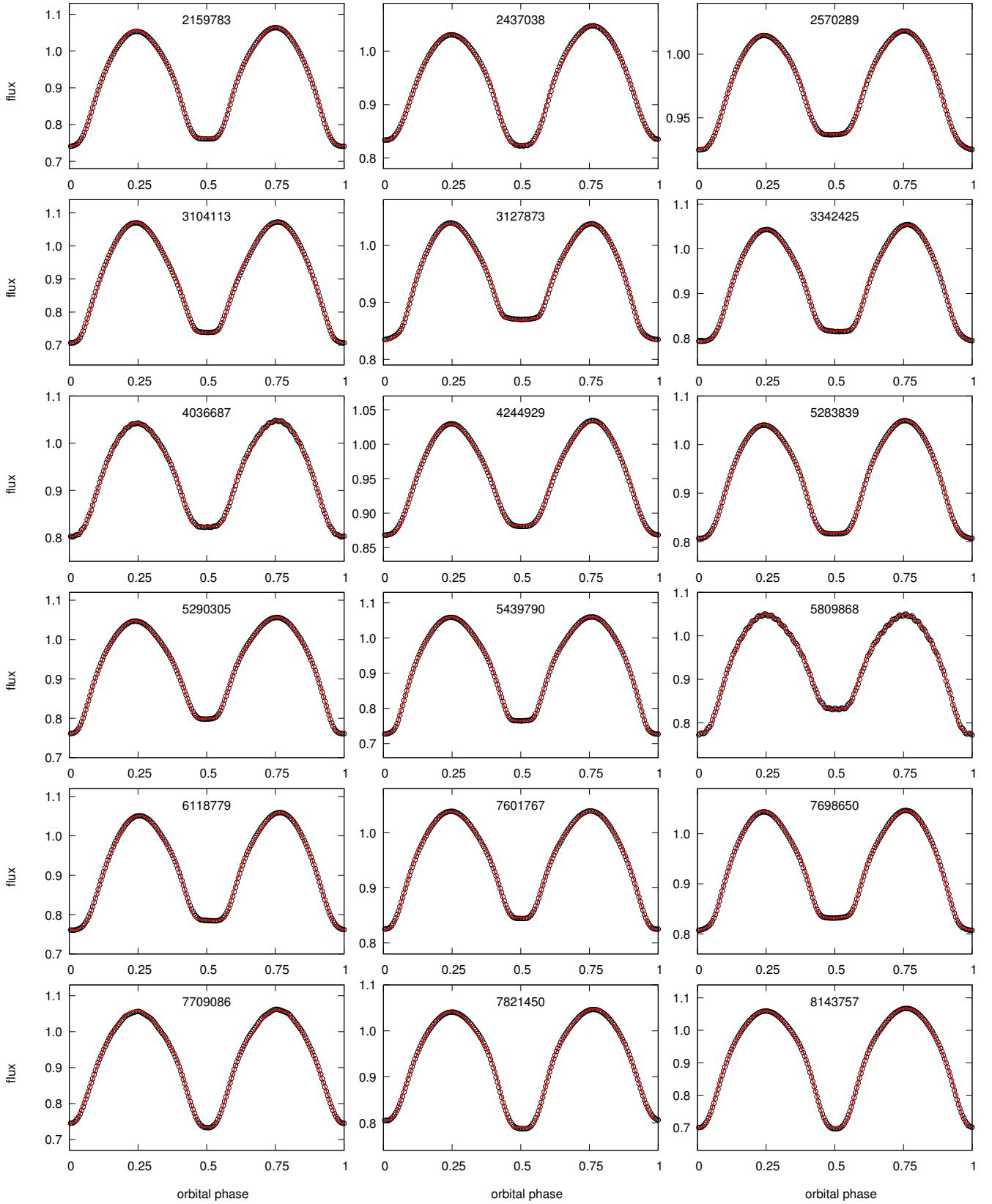


Figure B1. Lightcurves of the contact binaries studied in this work (open circles) superimposed with the best fitting models (red line). The number in each panel is the KIC number for a given object.

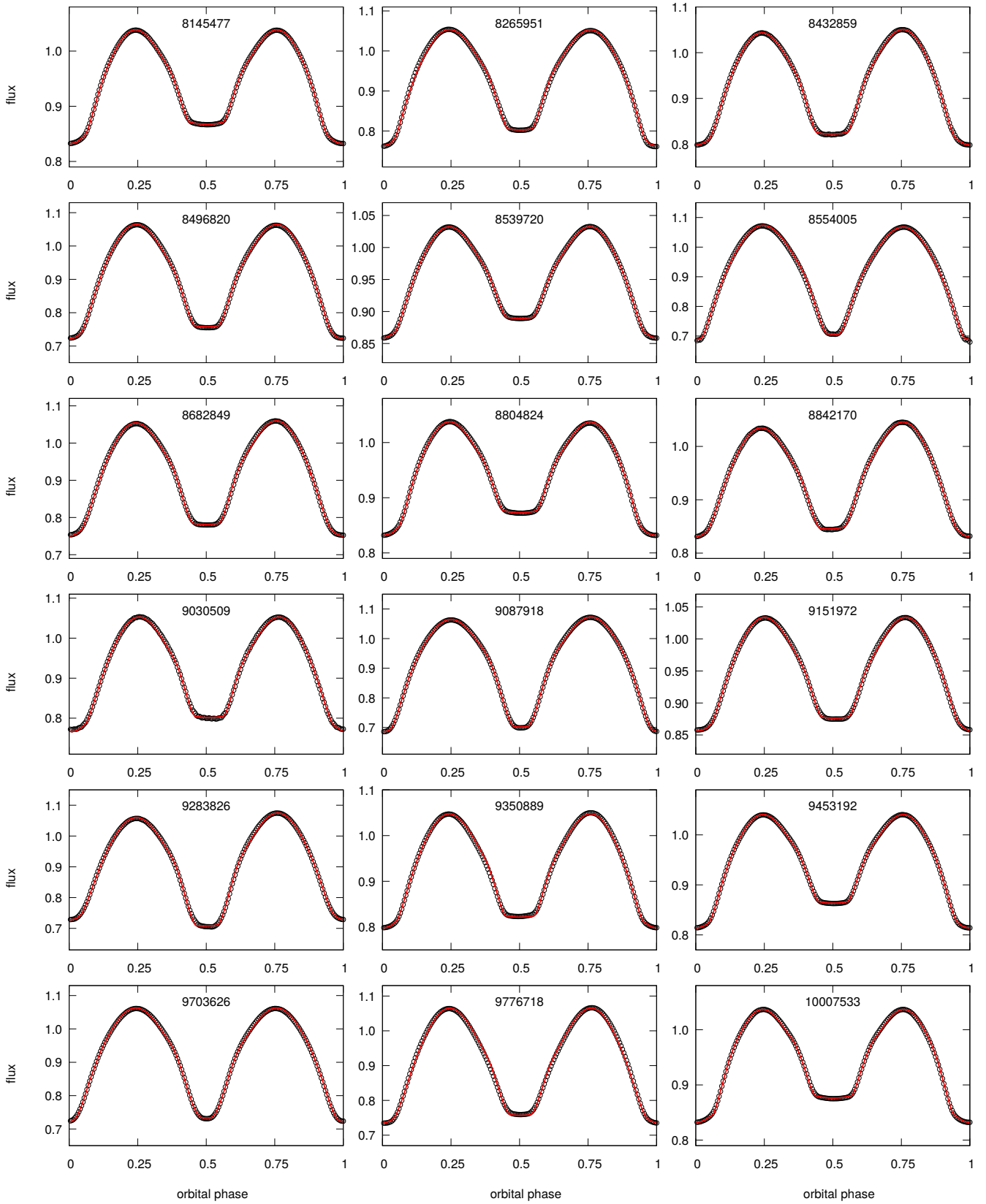


Figure B2. Lightcurves of the contact binaries studied in this work (open circles) superimposed with the best fitting models (red line). The number in each panel is the KIC number for a given object. Continuation of the Fig. B1.

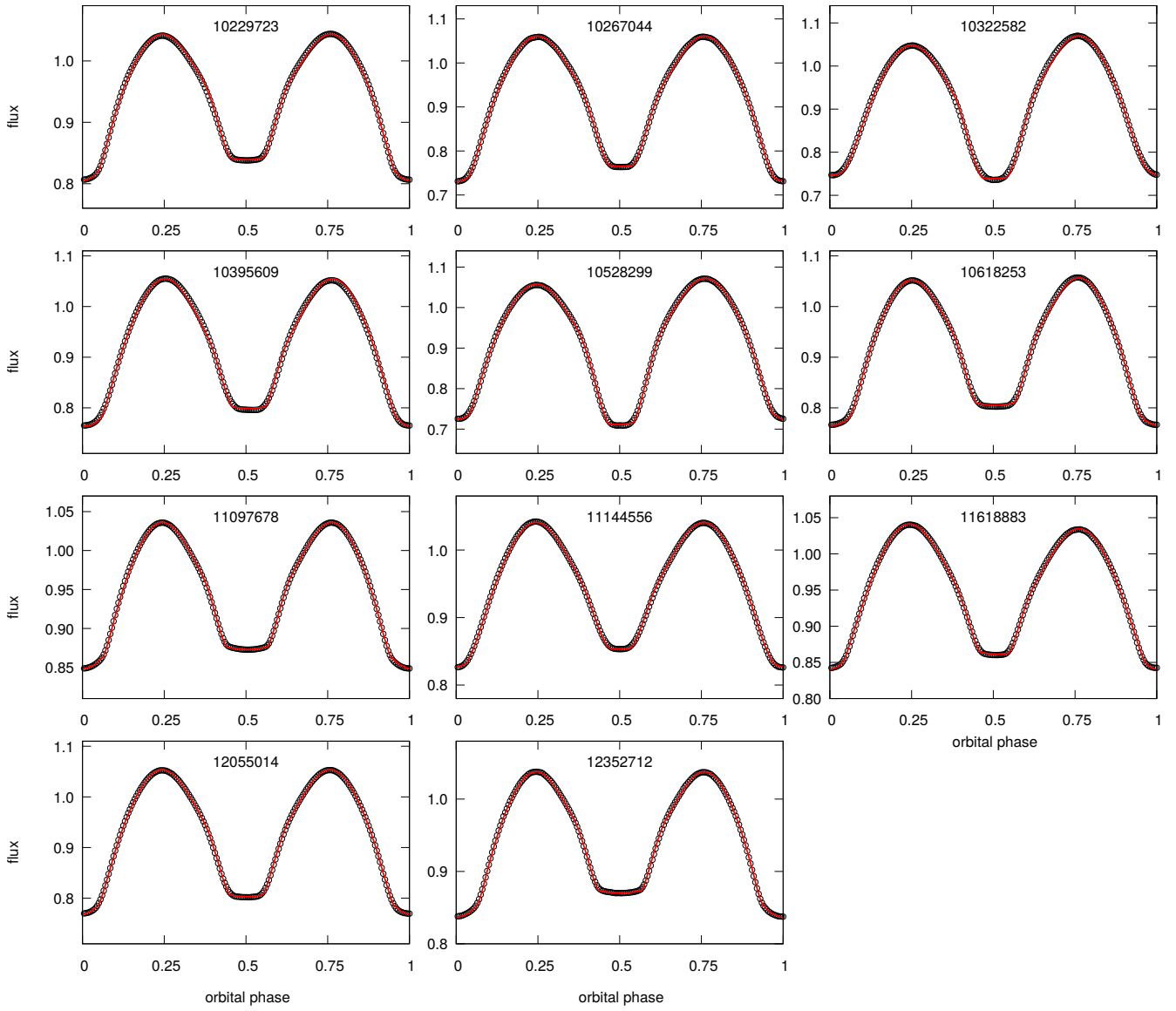


Figure B3. Lightcurves of the contact binaries studied in this work (open circles) superimposed with the best fitting models (red line). The number in each panel is the KIC number for a given object. Continuation of the Fig. B1.